



## Phononic Frequency Comb via Intrinsic Three-Wave Mixing

Adarsh Ganesan, Cuong Do, and Ashwin Seshia\*

Nanoscience Centre, University of Cambridge, Cambridge CB3 0FF, United Kingdom

(Received 3 October 2016; published 17 January 2017)

Optical frequency combs have resulted in significant advances in optical frequency metrology and found wide applications in precise physical measurements and molecular fingerprinting. A direct analogue of frequency combs in the phononic or acoustic domain has not been reported to date. In this Letter, we report the first clear experimental evidence for a phononic frequency comb. We show that the phononic frequency comb is generated through the intrinsic coupling of a driven phonon mode with an autoparametrically excited subharmonic mode. The experiments depict the comb generation process evidenced by a spectral response consisting of equally spaced discrete and phase coherent comb lines. Through systematic experiments at different drive frequencies and amplitudes, we portray the well-connected process of phononic frequency comb formation and define the attributes to control the features associated with comb formation in such a system. In addition to the demonstration of frequency comb, the interplay between the nonlinear resonances and the well-known Duffing phenomenon is also observed.

DOI: 10.1103/PhysRevLett.118.033903

A frequency comb consists of a series of equally spaced discrete frequencies. In recent years, optical frequency combs [1–8] have emerged as a potential toolset spanning diverse applications ranging from frequency metrology [1–4] to molecular fingerprinting [8]. Specifically, the ability to precisely define the frequency spacing between frequency markers and align these measurements with microwave sources through the comb generation process has led to a number of physical measurements [4] requiring very high accuracy including the observation of gravitational waves [9]. Optical frequency combs have been generated by using the comblike mode structure of mode-locked lasers and, more recently, through the interaction of continuous-wave lasers with high  $Q$  toroidal optical microresonators mediated via the Kerr nonlinearity [10].

Despite the analogies between phonons and photons, a direct analogue for an optical comb in the phononic domain has not been observed. However, theoretical work [11] has recently demonstrated the possibility for the generation of frequency combs in a phononic system represented by Fermi-Pasta-Ulam  $\alpha$  (FPU –  $\alpha$ ) chains [12]. Based on this theory, the phononic frequency comb can be generated only when a resonant mode is driven outside the dispersion band. However, it is a nontrivial experimental exercise to meet the comb excitation threshold with weaker signal levels associated with drive frequencies outside the dispersion band. In this Letter, we overcome this barrier by utilizing a piezoelectrically driven micromechanical resonator with improved electromechanical coupling leading to enhanced signal levels. This enables the first experimental realization of a phononic frequency comb in a microfabricated structure bearing similar traits to those predicted by numerical simulations performed on a FPU –  $\alpha$  chain [11]. Additionally, our resonator also captures the onset of Duffing nonlinear mechanism [13–15] and its interference with the nominal phononic comb.

The nonlinear three-wave mixing mechanism resulting in the generation of frequency combs is theoretically facilitated through the excitation of nonlinear resonances of various orders. Specifically, in direct nonlinear resonance (DNR) as termed in Ref. [11], the interaction between the eigenmode and driven phonon mode in a nonlinear lattice paves the way for the formation of equispaced spectral lines at a characteristic frequency  $\Delta\omega$  set by the drive frequency and the intrinsic phonon mode frequencies. Mathematically, the DNR phenomenon can be modeled through the coupled dynamics,

$$\begin{aligned} \ddot{Q}_1 = & -\omega_1^2 Q_1 - 2\zeta_1\omega_1 \dot{Q}_1 + f_d \cos(\omega_d t) + \alpha_{11} Q_1^2 \\ & + \beta_{111} Q_1^3 + \beta_{122} Q_1 Q_2^2, \end{aligned} \quad (1.1)$$

$$\begin{aligned} \ddot{Q}_2 = & -\omega_2^2 Q_2 - 2\zeta_2\omega_2 \dot{Q}_2 + \alpha_{12} Q_1 Q_2 \\ & + \alpha_{22} Q_2^2 + \beta_{112} Q_1^2 Q_2, \end{aligned} \quad (1.2)$$

where  $f_d$  is the displacement or drive level of drive tone  $\omega_d$ ,  $\alpha_{ij}$  and  $\beta_{ijk}$  are quadratic and cubic coupling coefficients, and  $\zeta_{i=1,2}$  are the damping coefficients. When the frequency of external driving  $\omega_d$  matches the resonant mode frequency  $\omega_1$  and at high enough values of drive, the resonant mode  $\omega_d$  and autoparametrically triggered subharmonic mode  $\omega_d/2$  are only excited with no additional spectral lines. Once the drive frequency  $\omega_d$  is set beyond the dispersion band, at high enough values of drive  $f_d$ , the mode  $Q_2$  is autoparametrically triggered at the frequency  $\omega_1/2$ . This, in turn, results in a response for  $Q_1$  at  $\omega_1$  and through higher-order nonlinear coupling between  $Q_1$  and  $Q_2$  as defined in Eqs. (1.1) and (1.2), the near-resonant terms of  $\cos(\omega_1 + p(\omega_d - \omega_1))t; p \in \mathbb{Z}$  are generated (see the Supplemental Material [16] Sec. S1 for the analysis).

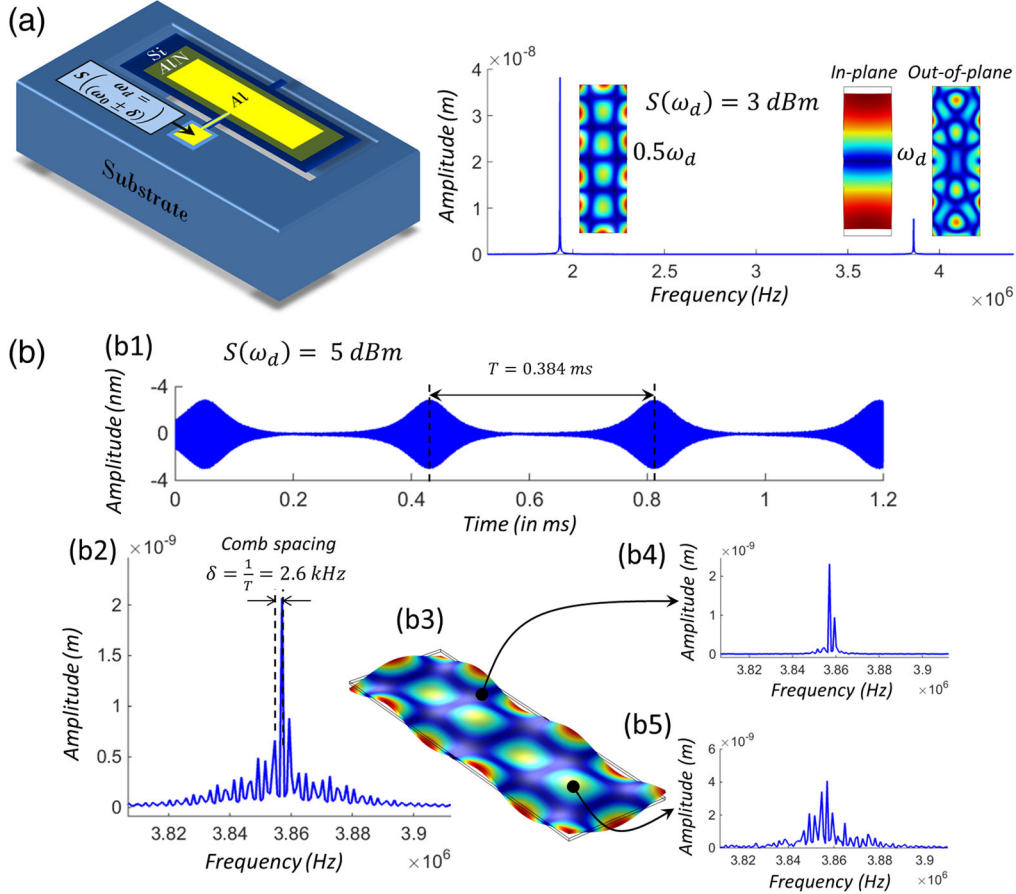


FIG. 1. Observation of the phononic frequency comb. (a) Left: Signal  $S(\omega_d)$  is applied on a free-free beam microstructure. Right: An intrinsic parametric excitation of the subharmonic mode (out of plane) at the drive power level 3 dBm of in-plane extensional mode. (b1) The pulse train corresponding to the phase coherent frequency comb at the drive power level 5 dBm, (b2) surface average displacement spectrum demonstrating comb formation, (b3) the subharmonic mode shape, (b4) the displacement at the node of the subharmonic mode indicating the absence of the frequency comb response, and (b5) the displacement at the antinode of the subharmonic mode indicating the presence of the frequency comb response.

The eigenmode excited at  $\omega_1$  is also referred to as the “comb mode” in this Letter.

To validate the aforementioned theory, a microscopic 1D extensional mode resonator of dimensions  $1100 \times 350 \times 11 \mu\text{m}^3$  has been considered as the experimental platform for this work [Fig. 1(a) and Supplemental Material [16] Fig. S1]. This structure is fabricated using a standard AlN-on-Si foundry process [17]. In this process, to start with, a  $0.5 \mu\text{m}$  thick AlN film is deposited on the SOI wafer. The AlN film is the transducer material employed in the piezoelectrically excited micromechanical device. To enable electrical interfacing, an additional Al metal layer of  $1 \mu\text{m}$  thickness is patterned. Finally, the bulk SOI wafer is etched by the deep reactive ion etching process to realize the freestanding microstructures. The fabricated Si chip ( $11 \times 11 \text{ mm}^2$ ) containing a micromechanical resonator is then electrically packaged in a ceramic leadless chip carrier (LCC44 Spectrum Semiconductors) for testing.

The piezoelectric resonator is then driven by electrical signals derived from a waveform generator (Agilent 335ARB1U) as shown in the Fig. 1(a), and the mechanical

response is optically recorded by a Polytec laser Doppler vibrometer (LDV). At an elevated drive level upon crossing a specific threshold value, the spectrum analyzer and LDV measurements prove the existence of an autoparametrically generated subharmonic mode [18] [Fig. 1(a)]. Here, the displacement profile corresponding to the subharmonic mode can be conceived as a prestressed framework for the level of coupling between the drive frequency and intrinsic resonance mode [Fig. 1(b)]. That being said, the propensity for comb generation is higher at the antinodes of the subharmonic mode. Additionally, Fig. 1(b1) provides evidence for the phase coherency of equidistant comb lines. In this Letter, we systematically report the experimental results carried out in the extensional resonator based test bed to understand the frequency comb generation and discuss the opportunities for active tuning of the comb structure.

The drive amplitude dependence on the phononic comb for an off-resonant drive frequency of 3.862 MHz is examined first [Fig. 2(A)]. Mere drive tone is present at low enough drive power levels  $< 3 \text{ dBm}$ . However, upon the drive power level meeting a certain threshold value of

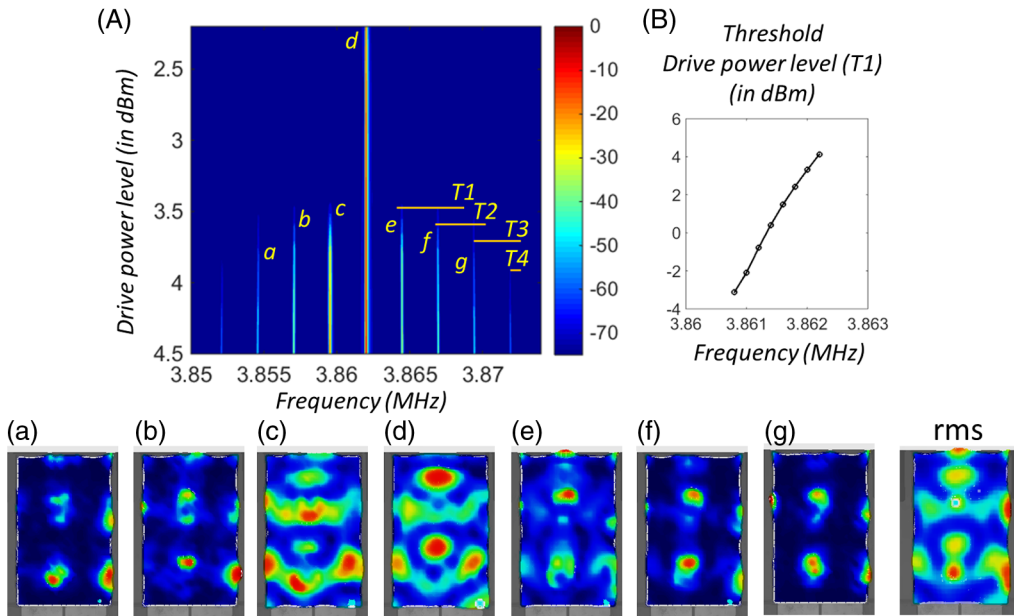


FIG. 2. High-order phononic frequency combs. (A) The drive power level-frequency contour indicating the thresholds  $T_1$ ,  $T_2$ ,  $T_3$ ,  $T_4$  for high-order frequency comb generation. (a)–(g) The out-of-plane displacement profiles at different frequencies on both sides of the dispersion curve. Here, Figs. 2(c) and 2(d) correspond to the nominal spatial vibration pattern of the comb mode, and Figs. 2(a) and 2(b) and 2(f) and 2(g) correspond to the spatial vibration pattern of the parametrically excited mode. rms: The rms displacement profiles in the frequency range 3.6–4.2 MHz at the drive frequency 3.862 MHz and drive power level = 4.5 dBm. (B) The threshold  $T_1$  as the drive frequency is detuned from resonance.

$\sim 3.5$  dBm, the comb eventually gets generated. With a further increase in drive power, the comb structure extends into higher orders. In other words, the spectral bandwidth of the frequency comb is directly related to the drive power level. In practice, such bandwidths for a particular drive power level can be expanded via design strategies to reduce the onset of the initiation threshold for parametric resonance [19]. The steps in Fig. 2(A) depict the existence of inherent thresholds for each higher-order spectral line. The dependence of the drive frequency on the comb generation thresholds is presented in Fig. 2(B). When the drive frequency is operated within the dispersion band ( $\sim 3.8590$  MHz) ( $< 3.8602$  MHz), the comb is not formed at even extreme power levels as high as 23.99 dBm. This exemplifies the absence of the comb generation pathway in the “dispersion band” regime. Nonetheless, outside this range  $> 3.8602$  MHz, the drive power level threshold and drive frequency follow a direct relationship, corresponding to the Lorentzian decay of the resonant peak. Figures 2(a)–2(g) show the underlying spatial manipulation of phonons from the spectral line  $\omega_d$  to the comb lines. Spatially, the phonons at the comb frequencies are present at the antinodes of the autoparametrically driven subharmonic mode [Figs. 2(a) and 2(b) and 2(e)–2(g)] with a concomitant reduction in the drive phonon population at these spatial locations [Fig. 2(d)]. Additionally, it is also interesting to note that the tone at the natural frequency  $\omega_1$  also takes up the comb-mode-specific spatial vibration pattern [Fig. 2(c)]. In other words, the tone at  $\omega_1$  is always excited along with the drive tone  $\omega_d$  during the comb generation process.

Hence, the reported frequency comb mechanism can enable a new approach for resonance frequency estimation in micro- and nano-mechanical resonant sensors.

Under high enough drive amplitude conditions ( $> \sim 5$  dBm), there is evidence of the Duffing nonlinear mechanism or fold-over effect [Fig. 3(a)] [13–15]. Here, the frequency of the driven mode is amplitude dependent, which results in increased comb spacing corresponding to the drive amplitude [Fig. 3(a)]. To study the dependence of “detuning” of the drive tone on both DNR and Duffing influenced DNR regimes, the underlying frequency responses have to be juxtaposed. Yet, at a constant drive power level, the number of comb lines produced can be dependent on the detuning level of the drive. Hence, the nature of the comb structure for different detuning levels cannot be directly compared. Alternatively, by standardizing to five comb lines, the resulting frequency contours are obtained [Figs. 3(b) and 3(d)]. This standardization, however, results in the Duffing phenomenon at higher drive frequencies  $> 3.8622$  MHz, as the higher threshold for reaching five comb lines directly meets the Duffing criterion [Figs. 3(b) and 3(d)]. In DNR, the far-detuned drive frequency results in larger comb spacing [Fig. 3(d)]. In contrast, the comb spacing in Duffing influenced DNR remains the same, and the overall comb collectively gets shifted with the drive frequency shift. This crossover can be explained by the fold over of the resonant peak resulting in frequency renormalization ( $\tilde{\omega}_0$ ) [11]. The influence of the Duffing mechanism on the nominal DNR is guided by the intrinsic Duffing and DNR thresholds. An active tuning of these attributes in a microstructure [20] will

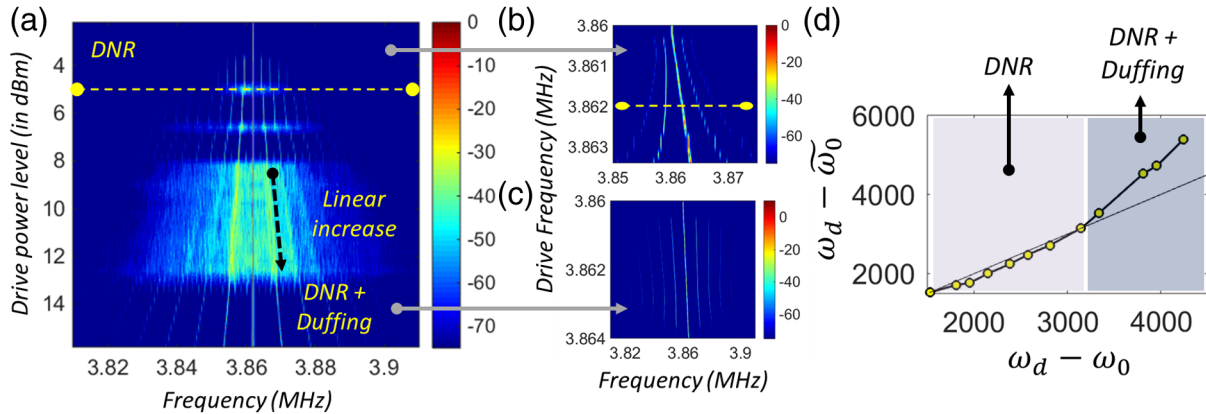


FIG. 3. Interplay between the DNR and Duffing mechanisms. (a) The drive power level-frequency contour (drive frequency = 3.862 MHz) indicating the DNR and DNR-Duffing regimes. (b), (c) The drive frequency-sense frequency contour (five comb lines) in the DNR and DNR-Duffing regimes, respectively. (d) The comb spacing with frequency renormalization ( $\omega_d - \tilde{\omega}_0$ ) vs the comb spacing without frequency renormalization ( $\omega_d - \omega_0$ ) indicating the DNR and Duffing regimes.

enable independent control over both DNR and Duffing mechanisms and consequent tailoring of the frequency comb in both regimes. In Fig. 3(a), there is additional evidence for the “filling in” of multiple spectral lines within the comb (cyan regions) in the Duffing influenced DNR regime. This intriguing high-generation comb phenomenon needs investigation, even though this result falls out of the scope of this Letter.

While the individual amplitude and frequency dependences are explored in both DNR and DNR-Duffing regimes, the interplay between these two parameters also reveals an additional intriguing property. As seen before, the frequency detuning threshold for frequency comb generation is dependent on the dispersion bandwidth. Within the dispersion band, the comb is not generated. Outside the band, the amplitude required for comb generation continuously increases as the drive frequency is increasingly spaced away from the resonance. This clearly signifies that the quality factor of the resonance peak and resonant transconductance are strong determinants of frequency comb generation. A microstructure with a tunable quality factor and transconductance [21] can, therefore, enable active control over the dynamics of phononic comb generation.

We now present a brief discussion on the dependence of the spectral bandwidth corresponding to the frequency comb with the drive power level and detuning. For a given detuning level, the bandwidth increases in discrete steps with the drive power level. However, there exists a nontrivial relationship between the bandwidth and detuning level. A far-detuned frequency comb, in spite of having a larger comb width, will only have fewer comb lines. On the other hand, a near-detuned frequency comb, in spite of having a larger comb density, has a smaller comb width. Therefore, to achieve an optimal spectral bandwidth, the trade-off between the comb density and width must be resolved. From a technological perspective, such comb bandwidths can potentially be increased through parametric resonator design strategies and reduced damping conditions [19].

Figure 4(a) maps the “dispersion band,” “phononic comb,” and “small signal” regimes in the driving response. For studying the underlying spatial aspects in each of these regimes, the rms surface displacement averaged over the frequency range of 3.6 to 4.2 MHz (using LDV measurements) is compared. Figure 4(b) shows the rms vibration patterns for different drive frequencies. In the dispersion band (at 3.858 MHz), since there is no comb formation, the resonant mode shape is not altered, and, hence, the comb-mode-specific vibration pattern is only observed. Contrary to this, in the phononic comb regime (at 3.856 and 3.862 MHz), the subharmonic-mode-specific vibration pattern is observed following the phonon manipulation from the drive frequency to the comb spectral lines [Figs. 2(a)–2(g)]. In the small signal regime, similar to the dispersion band, the comb is not formed at normal drive levels, and the resonant mode pattern is preserved. To understand the relevance of drive power levels on the spatial aspects of comb formation, the underlying rms vibration patterns corresponding to drive frequency 3.862 MHz are compared. As seen in Fig. 4(c), the rms vibration patterns gradually shift from the comb-mode-specific to the subharmonic-mode-specific vibration pattern following phonon manipulation.

We now recapitulate the traits concomitant with the different regimes of operation in the phononic comb. In the dispersion band regime, there is no comb formation. Therefore, only the tones corresponding to  $\omega_d$  and  $\omega_d/2$  are observed. Also, the rms spatial displacement pattern around  $\omega_d$  corresponds to the comb-specific vibration pattern [Fig. 4(b)]. In the phononic comb regime, additional spectral lines are also observed around  $\omega_d$  and, hence, the rms spatial displacement pattern around  $\omega_d$  corresponds to a merger of the comb-mode-specific vibration pattern and the parametrically excited subharmonic-mode-specific vibration pattern [Fig. 4(b)]. In the small signal regime, comb excitation is not observed, and only the tone  $\omega_d$  is visible. The rms spatial displacement pattern around  $\omega_d$

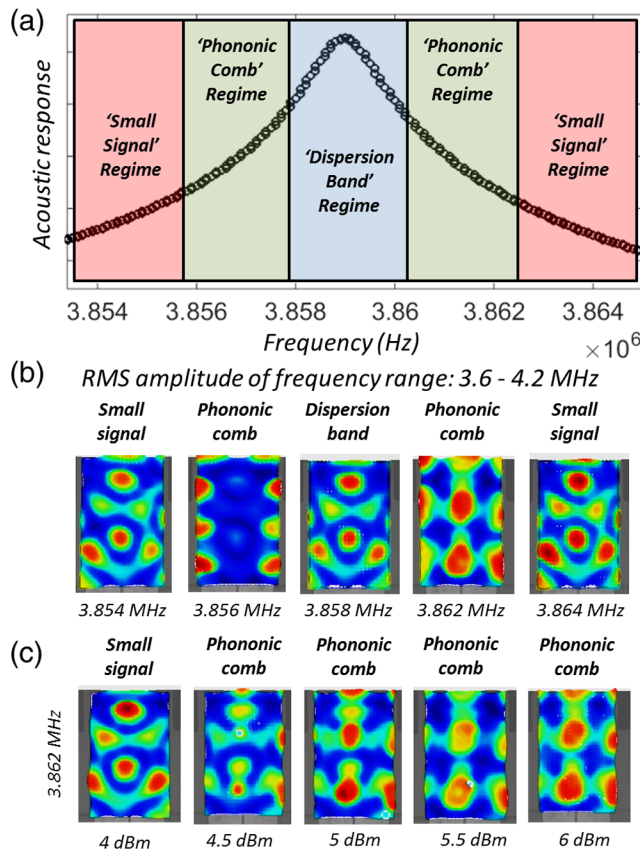


FIG. 4. Regime of the phononic comb formation. (a) Phononic comb regime falling just outside the dispersion band of the mechanical mode. (b), (c) The rms displacement profiles in the frequency range 3.6–4.2 MHz at different drive frequencies (drive power level = 6 dBm) and drive amplitudes ( $\omega_d = 3.862$  MHz), respectively.

corresponds to the weak excitation of the comb-mode-specific vibration pattern [Fig. 4(b)].

While the behavior of comb generation in different regimes is now understood, a brief discussion on the frequency ranges corresponding to each regime is presented here. As the comb generation thresholds at higher drive levels are met for a wide range of frequencies, the frequency range of the phononic comb regime expands with the drive level, and, consequently, the frequency range of the small signal regime diminishes. However, in our experiments, the frequency range of the dispersion band regime stays almost constant with the drive level. Despite this, in practice, the dispersion bandwidth can be controlled through several exquisite engineering approaches [20,21].

In summary, this Letter reports the first ever experimental demonstration of a phononic frequency comb. Further, a phenomenological model is specified to define the nature of direct nonlinear resonances that govern frequency comb generation. The presented concepts find general relevance to other nonlinear systems in both quantum and classical domains. In addition to the fundamental advance reported here, phononic frequency combs also find applications to accurate micro- and nano-mechanical resonant sensors

adapted for stable long-duration measurements [22,23], engineering phase-coherent phonon lasers [24], phonon computing [25,26], pulse train mediated ultrasonic imaging, and fundamental investigations of nonlinear phononics [27].

Funding from the Cambridge Trusts is gratefully acknowledged.

\*aas41@cam.ac.uk

- [1] T. Udem, R. Holzwarth, and T. W. Hansch, *Nature (London)* **416**, 233 (2002).
- [2] P. Del'Haye, A. Schliesser, O. Arcizet, T. Wilken, R. Holzwarth, and T. J. Kippenberg, *Nature (London)* **450**, 1214 (2007).
- [3] T. J. Kippenberg, R. Holzwarth, and S. A. Diddams, *Science* **332**, 555 (2011).
- [4] J. Ye, H. Schnatz, and L. W. Hollberg, *IEEE J. Sel. Top. Quantum Electron.* **9**, 1041 (2003).
- [5] R. Holzwarth, T. Udem, T. W. Hansch, J. C. Knight, W. J. Wadsworth, and P. S. J. Russell, *Phys. Rev. Lett.* **85**, 2264 (2000).
- [6] R. J. Jones and J.-C. Diels, *Phys. Rev. Lett.* **86**, 3288 (2001).
- [7] D. J. Jones *et al.*, *Science* **288**, 635 (2000).
- [8] M. J. Thorpe *et al.*, *Science* **311**, 1595 (2006).
- [9] B. P. Abbott *et al.*, *Phys. Rev. Lett.* **116**, 061102 (2016).
- [10] T. J. Kippenberg, S. M. Spillane, and K. J. Vahala, *Phys. Rev. Lett.* **93**, 083904 (2004).
- [11] L. S. Cao, D. X. Qi, R. W. Peng, M. Wang, and P. Schmelcher, *Phys. Rev. Lett.* **112**, 075505 (2014).
- [12] E. Fermi, J. Pasta, and S. Ulam, Los Alamos Report No. LA-1940 978, 1955.
- [13] I. Kovacic and M. J. Brennan, *The Duffing Equation: Nonlinear Oscillators and Their Behaviour* (John Wiley & Sons, New York, 2011).
- [14] J. S. Aldridge and A. N. Cleland, *Phys. Rev. Lett.* **94**, 156403 (2005).
- [15] A. Eichler, J. Moser, J. Chaste, M. Zdrojek, I. Wilson-Rae, and A. Bachto, *Nat. Nanotechnol.* **6**, 339 (2011).
- [16] See Supplemental Material at <http://link.aps.org/supplemental/10.1103/PhysRevLett.118.033903> for the analytical derivation of DNR frequency comb and device operation.
- [17] L. L. P. Wong *et al.*, *Sens. Actuators A Phys.* **247**, 430 (2016).
- [18] G. M. Chechin, N. V. Novikova, and A. A. Abramenko, *Physica (Amsterdam)* **166D**, 208 (2002).
- [19] Y. Jia, S. Du, and A. A. Seshia, *Sci. Rep.* **6**, 30167 (2016).
- [20] I. Kozinsky, H. W. Ch. Postma, I. Bargatin, and M. L. Roukes, *Appl. Phys. Lett.* **88**, 253101 (2006).
- [21] S. S. Verbridge, D. F. Shapiro, H. G. Craighead, and J. M. Parpia, *Nano Lett.* **7**, 1728 (2007).
- [22] R. P. Middlemiss, A. Samarelli, D. J. Paul, J. Hough, S. Rowan, and G. D. Hammond, *Nature (London)* **531**, 614 (2016).
- [23] A. N. Cleland and M. L. Roukes, *Nature (London)* **392**, 160 (1998).
- [24] K. Vahala, M. Herrmann, S. Knünz, V. Batteiger, G. Saathoff, T. W. Hänsch, and Th. Udem, *Nat. Phys.* **5**, 682 (2009).
- [25] L. Wang and B. Li, *Phys. Rev. Lett.* **99**, 177208 (2007).
- [26] K. Stannigel, P. Komar, S. J. M. Habraken, S. D. Bennett, M. D. Lukin, P. Zoller, and P. Rabl, *Phys. Rev. Lett.* **109**, 013603 (2012).
- [27] M. Först, C. Manzoni, S. Kaiser, Y. Tomioka, Y. Tokura, R. Merlin, and A. Cavalleri, *Nat. Phys.* **7**, 854 (2011).